CHEMISTRY OF MATERIALS

ARTICLE

pubs.acs.org/cm

Structural Origin of Overcharge-Induced Thermal Instability of Ni-Containing Layered-Cathodes for High-Energy-Density Lithium Batteries

Lijun Wu,[†] Kyung-Wan Nam,[†] Xiaojian Wang,[†] Yongning Zhou,[†] Jin-Cheng Zheng,[‡] Xiao-Qing Yang,*[,†] and Yimei Zhu*[,†]

[†]Brookhaven National Laboratory, Upton, New York 11973, United States

[‡]Department of Physics, Xiamen University, Xiamen, 361005, China

Supporting Information

ABSTRACT: Using a combination of time-resolved X-ray diffraction (XRD), in situ transmission electron microscopy (TEM), and first principles calculations, we explore the structural origin of the overcharge induced thermal instability of two cathode materials, $LiNi_{0.8}Co_{0.15}Al_{0.05}O_2$ and $LiNi_{1/3}Co_{1/3}Mn_{1/3}O_2$, which exhibit significant difference in thermal stabilities. Detailed TEM analysis reveals, for the first time, a complex core−shell-surface structure of the particles in both materials that was not previously detected by XRD. Structural comparison indicates that the overcharged $Li_xNi_{0.8}Co_{0.15}Al_{0.05}O_2$ ($x < 0.15$) particles consist of a rhombohedral core, a spinel shell, and a rock-salt structure at the surface, while the overcharged $Li_xNi_{1/3}Co_{1/3}Mn_{1/3}O_2$ consists of a similar core−shell-surface structure but a very different CdI_2-type surface structure. The thermal instability of $Li_xNi_{0.8}Co_{0.15}Al_{0.05}O_2$ can be attributed to the release of oxygen because of the rapid growth of the rock-salt-type structure on the surface during heating. In contrast, the CdI_2-type surface structure of the overcharged $Li_xNi_{1/3}Co_{1/3}Mn_{1/3}O_2$ particles delays the oxygen-release reaction to a much higher temperature resulting in better stability. These results gave deep insight into the relationship between the local structural changes and the thermal stability of cathode materials, which is vital to the development of new cathode materials for the next generation of lithium-ion batteries.

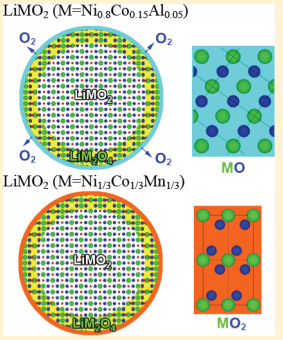

KEYWORDS: lithium batteries, thermal stability, high capacity cathode, in situ, TEM, XRD

INTRODUCTION

The lithium-ion battery is the dominating rechargeable power-source for cell phones, laptop computers, and other mobile computing- and communication-devices. In addition, it is the most promising power source for electric vehicles (EV) and hybrid electric vehicles (HEV). The development of new electrode materials for the next generation of lithium-ion batteries for EV applications with higher energy density, longer life, and better safety[1] is still stagnating and requires systematic in situ studies of the structural changes of the electrode materials during charge−discharge cycling, aging, and thermal decomposition. The information obtained from these studies is vital for developing new electrodes as well as for improving their performance in today's commercial lithium-ion batteries. Previous studies include the use of various in situ and ex situ spectroscopic techniques, such as X-ray and neutron diffraction,[2−5] X-ray absorption (XAS),[6,7] and nuclear magnetic resonance (NMR).[8,9] These techniques are powerful in investigating structural changes through the entire electrodes but inadequate in exploring the microscopical origin of the changes and where and how the new structure nucleated and propagated during the electrochemical cycles and heating. Hence, in situ spectroscopic techniques with high spatial resolution and location specificity are very much needed. High-resolution transmission electron microscopy (HRTEM) offers both local structure and chemical information for these phase transitions.[10] However, HRTEM has its own drawback with limited sampling of the sample and poor statistics; thus, if used alone, the information of structure changes it provides may not reflect the structure change of the entire sample, unless other volume-averaged in situ spectroscopy methods are used. In this paper, we report the first in situ TEM studies on the structural changes of two important cathode materials, $LiNi_{0.8}Co_{0.15}Al_{0.05}O_2$ and $LiNi_{1/3}Co_{1/3}Mn_{1/3}O_2$ at overcharged states during heating. We carried out time-resolved in situ XRD studies during heating for these materials in parallel with our TEM study. The XRD results present a roadmap on the structure change on a global level for the phase transitions, while TEM experiments give local details about where the nucleation of the new phases occurs and how the new phases propagate under overcharged states during heating. The combination of these two techniques provides a unique opportunity to understand the structural origin of the thermal stability related to the overcharge. It also offers useful guidance in developing new in situ TEM techniques for research on battery materials.

Received: May 23, 2011
Revised: July 19, 2011
Published: August 04, 2011

The Ni-rich layer-structured cathode materials, such as $LiNi_{0.8}Co_{0.15}Al_{0.05}O_2$, are good candidates for the new generation of Li-ion batteries, especially as power sources for EV and HEV applications, because of their high energy-density and low cost.[11,12] In December 2009, Panasonic, one of the leading lithium-ion battery manufacturers, announced their successful formulation of a new high-capacity (3.1 Ah) 18650 Li-ion cell using a Ni- based cathode material, similar to $LiNi_{0.8}Co_{0.15}Al_{0.05}O_2$. This development demonstrated the great potential of this type of material and warranted an in-depth study of these materials that will undoubtedly provide important information in formulating high capacity cells. However, one troubling issue in using Ni-rich cathode materials is their thermal instability that might jeopardize safety during thermal runaway. It was reported that at highly delithiated states (overcharged), the reduction of Ni^{4+} during heating releases oxygen that can accelerate severe thermal runaway by reacting with the electrolyte and leads to catastrophic failure of the battery.[13−17] The NiO with the rock-salt structure formed at the surface of the electrode through the reduction of Ni^{4+} also causes a rise in the impedance of the cathode during cycling, which degrades the cycle capacity of the battery.[18−21] Therefore, more thermal stable cathode materials with reduced Ni concentration, for example, $LiNi_{1/3}Co_{1/3}Mn_{1/3}O_2$, have been developed.[22,23] Thermal gravimetric analysis (TGA) reveals that the $Li_{0.55}Ni_{1/3}Co_{1.3}Mn_{1/3}O_2$ powders start releasing oxygen at higher temperatures and have much less oxygen loss in comparison with the $Li_{0.45}Ni_{0.8}Co_{0.15}Al_{0.05}O_2$ powders.[14,24] The differential scanning calorimetry (DSC) also shows that the former has higher onset temperature and lower heat generation than the latter, indicating much better thermal stability. Unfortunately, this higher thermal stability is obtained at the expense of energy density. Recently, a concentration-gradient cathode material based on layered Li−Ni−Co−Mn oxides showed not only high energy density but also excellent cycling and safety characteristics.[25] XRD,[14,24] including time-resolved XRD during heating,[4] has associated the oxygen release of the Ni-based layered cathodes with several structural transformations, including $R\bar{3}m$ (layered) → $Fd3m$ (spinel) → $Fm3m$ (rock-salt) transitions, especially the last one to rock-salt structure. However, little work on the nucleation, growth, and the distribution of the new phases during phase transitions has been reported. Combining HRTEM imaging with selected-area electron diffraction (SAED) at a wide range of temperatures 25−450 °C (533 °C for $LiNi_{1/3}Co_{1/3}Mn_{1/3}O_2$), we systematically investigated the local structural changes in overcharged $Li_xNi_{0.8}Co_{0.15}Al_{0.05}O_2$ and $Li_xNi_{1/3}Co_{1/3}Mn_{1/3}O_2$ cathode materials. Our findings offer a complete picture on where and how the new structures are nucleated and evolved locally on the different phase-transition paths of these two materials. These results provide valuable information about the role of each transition metal (Ni, Co, and Mn) on the thermal- and structural-instability of the materials during overcharging and heating and are applicable to the development of new cathode materials with a similar layered structure and high capacity and thermal stability.

EXPERIMENTAL SECTION

The cathodes consist of 84% active materials (i.e., $LiNi_{0.8}Co_{015}Al_{0.05}O_2$ (Fuji Chemical) or $LiNi_{1/3}Co_{1/3}Mn_{1/3}O_2$ (Seimi, Japan)), 8% carbon black (Chevron), and 8% PVDF (Kureha). They were incorporated into a battery cell with a Li metal-foil anode, a Celgard separator,

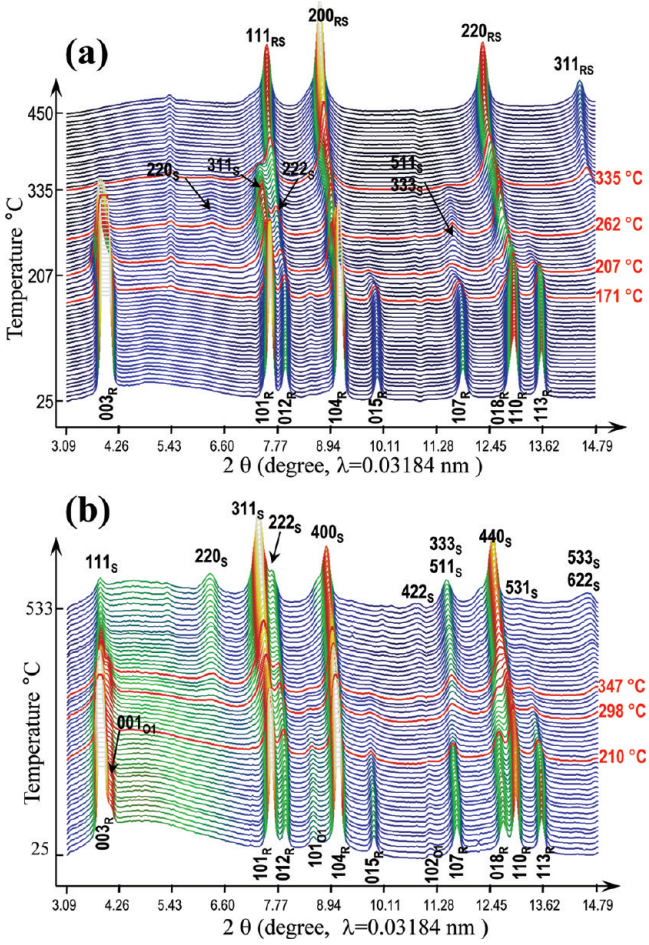

Figure 1. Time-resolved XRD patterns of overcharged $Li_xNi_{0.8}Co_{0.15}Al_{0.05}O_2$ (a), and $Li_xNi_{1/3}Co_{1/3}Mn_{1/3}O_2$ (b) in the absence of electrolyte. The intensity profiles are drawn in color for clarity with those taken at key temperatures in red color.

and a 1.2 M $LiPF_6$ solution in a 3:7 EC (ethyl carbonate)/DMC (dimethyl carbonate) solvent as the electrolyte. The cell was charged at a C/18 rate to 4.8 V, which reduced Li concentration to 0.15 based on the total charge involved. The cell was then held at 4.8 V for 1 h to obtain the overcharged state before transferring to a glovebox for disassembly. The Li concentration for overcharge state was therefore slightly less than 0.15. The overcharged cathode (on the Al current collector) was rinsed in DMC solvent to eliminate residual salts. For time-resolved X-ray diffraction, we scratched off the cathode materials from the current collector and loaded them into 0.5 mm-diameter quartz capillaries in a glovebox. After hermetically sealing the capillaries, we mounted them on the thermal stage of the beamline X7B at National Synchrotron Light Source (NSLS), Brookhaven National Laboratory. Diffraction patterns were collected continuously using a Mar-345 image plate detector in the transmission mode while heating the capillaries to 600 °C. The wavelength used was 0.3184 Å. For the TEM experiments, we loaded the overcharged cathode particles scraped from the current collector into a small glass bottle filled with small volume of acetone to disperse them. Supersonic vibration ensured that the particles were dispersed well before dropping the sample on a TEM carbon grid. We carried out HRTEM and electron diffraction using the JEM-3000F microscope operated at 300 KV. The microscope is equipped with an ultrahigh-resolution objective-lens pole-piece and a Gatan double-tilt heating stage capable of measuring temperature in 1 °C accuracy. The

dx.doi.org/10.1021/cm201452q |Chem. Mater. 2011, 23, 3953–3960

overcharged sample is structurally stable in the high vacuum environment (3×10^{-5} Pa) in TEM at room temperature. We always use low beam current and short exposure-time for image recording to ensure no electron beam induced structural change. The HRTEM images were simulated using homemade computer codes based on the multislice method.

The first principle calculations were performed using an ultrasoft pseudopotential method based on density functional theory (DFT), as implemented in Quantum ESPRESSO.[26] Appropriate k-point meshes and energy cutoff of 40 hartree were chosen to ensure the convergence of the self-consistent calculation. Nonmagnetic, ferromagnetic, and antiferromagnetic solutions were considered in the calculations. General gradient approximation (GGA) was used for exchange-correlation functional, the correction for binding energy of O_2 molecule, and the correction of GGA+U treatments were considered in the calculations.

RESULTS AND DISCUSSIONS

(a). Time-Resolved XRD. Figure 1a shows a series of time-resolved XRD patterns of the overcharged $Li_xNi_{0.8}Co_{0.15}Al_{0.05}O_2$ particles ($x < 0.15$) from room temperature to 450 °C in the absence of the electrolyte. The XRD shows that the as-overcharged $Li_xNi_{0.8}Co_{0.15}Al_{0.05}O_2$ particles have a rhombohedral structure with the lattice parameter c = 1.386 nm. The phase transition from the rhombohedral to the spinel phase starts at about 171 °C and is completed at about 207 °C, both values being lower than those of the fully charged $Li_{0.27}Ni_{0.8}Co_{0.15}Al_{0.05}O_2$. The phase transition from spinel to the rock-salt phase starts at about 262 °C and finishes at about 335 °C, as indicated by the decrease in intensity of the 311 and 511 (333) peaks of the spinel phase.

The time-resolved XRD for the overcharged $Li_xNi_{1/3}Co_{1/3}Mn_{1/3}O_2$ (Figure 1b) also shows some different phase-transition behaviors compared to the fully charged $Li_{0.33}Ni_{1/3}Co_{1/3}Mn_{1/3}O_2$.[27] Although the rhombohedral is still the dominant phase up to 210 °C, a new phase appeared as indicated by the additional weak peaks that are indexed with a CdI_2-type structure (denoted as O1). The phase transition of the rhombohedral to the spinel phase of the overcharged $Li_xNi_{1/3}Co_{1/3}Mn_{1/3}O_2$ starts at about 210 °C and is completed at about 347 °C, which is significantly higher than those of the overcharged $Li_xNi_{0.8}Co_{0.15}Al_{0.05}O_2$. Similar to the fully charged $Li_{0.33}Ni_{1/3}Co_{1/3}Mn_{1/3}O_2$, the spinel structure of the overcharged $Li_xNi_{1/3}Co_{1/3}Mn_{1/3}O_2$ undergoes another phase transition when heated above 298 °C, as indicated by the gradually increased intensities of the 220 and 422 peaks with the rise of temperature. XRD analysis (see Supporting Information, Figure S1) points out that the increased intensities of the 220 and 422 peaks are due to the partial occupancy of the transition metals (Ni, Co, and Mn) at the Li sites (Wyckoff position 8a). For convenience, we refer this kind of structure as M_3O_4 (M = $Ni_{1/3}Co_{1/3}Mn_{1/3}$) type spinel,[27] to distinguish with LiM_2O_4-type spinel structure in which no transition metals occupy at Li site. This M_3O_4 type spinel structure pushes the phase transition to a rock-salt structure at a higher temperature.

(b). In Situ TEM. *Overcharged $Li_xNi_{0.8}Co_{0.15}Al_{0.05}O_2$ Particles.* Overall examination of the overcharged $Li_xNi_{0.8}Co_{0.15}Al_{0.05}O_2$ particles reveals that the particle sizes range from several hundreds of nanometers to a couple of micrometers. Figure 2a shows a typical low-magnification bright-field TEM image with the corresponding selected area electron-diffraction pattern (SAEDP) with a selected area of about 240 nm in diameter

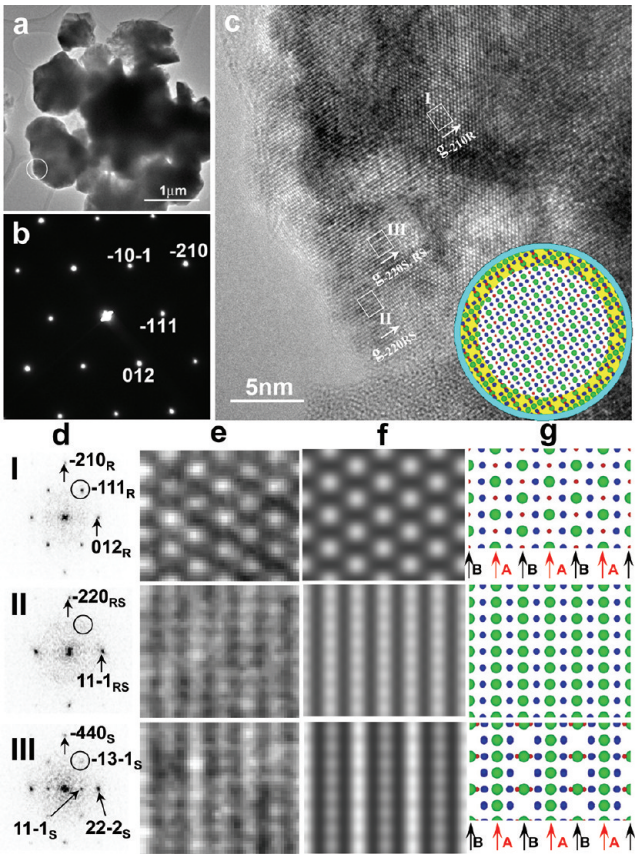

Figure 2. (a) Bright-field image from overcharged $Li_xNi_{0.8}Co_{0.15}Al_{0.05}O_2$ particles. (b–c) SAEDP (b) and HRTEM image (c) from the circled area in (a). The inset in (c) is the schematic drawing of the complex core–shell-surface structure of the overcharged particle with the rhombohedral in the core, spinel in the shell, and rock-salt at the surface. (I–III) First column (d) and second column (e): Diffractograms (first column) and magnified images (second column) from areas I, II, and III. The third column (f) contains the calculated images with the defocus being 9 nm, and the thickness being 11, 8, and 9.8 nm respectively for I, II, and III. The fourth column (g) has the projections of the rhombohedral-, rock-salt-, and spinel-structures along the I: $[-1-21]_R$, II: $[112]_{RS}$, and III: $[112]_S$ directions. The red, green, and blue balls represent Li, Ni (Co, Al), and O, respectively. The subscript R, S, and RS denote rhombohedral, spinel, and rock-salt structure, respectively.

shown in Figure 2b. The SAEDP has a pseudohexagonal pattern and can be indexed as the $[-1-21]_R$ diffraction pattern of the rhombohedral (subscript R denotes rhombohedral). This result agrees very well with our time-resolved XRD study for the same sample before heating, showing that, when averaged over a 240 nm diameter area in SAEDP, the structural information obtained is the same as that in XRD averaging 1 mm^2 sample area (the area of the X-ray beam). Figure 2c shows the HRTEM image taken from the edge of the circled area in Figure 2a; there are three different types of areas, marked as I, II, and III rectangles. The diffractogram (Fourier transform of the image) from area I (first column in Figure 2-I, denoted as Figure 2-I-d) is similar to that of the SAEDP shown in Figure 2b, indicating that the structure is rhombohedral. The magnified HRTEM image, Figure 2-I-e, also has a pseudohexagonal pattern, is consistent with the arrangement of the cations in the $[-1-21]_R$ projection of the rhombohedral structure (Figure 2-I-g). Image simulation

dx.doi.org/10.1021/cm201452q |*Chem. Mater.* 2011, 23, 3953–3960

(Figure 2-I-f) based on the rhombohedral structure closely agrees with the experimental image in Figure 2-I-e. (please note that although area I has the same rhombohedral structure as in the bulk, it was not located in the core part of the particle. It is a nanosized domain with rhombohedral structure located in a mixed domain area referred as "shell" in this paper). However, the diffractogram in Figure 2-II-d and image in Figure 2-II-e of the area II are quite different from those of the area I. The diffractogram for area II can only be indexed as the $[112]_{RS}$ pattern of the rock-salt type structure (denoted with a subscript RS). The HRTEM image of area II (Figure 2-II-e) depicts a rectangular pattern, and is consistent with the arrangement of cations in the $[112]_{RS}$ projection of the rock-salt structure (Figure 2-II-g). Our image simulation (Figure 2-II-f) based on the structure of rock-salt matches well with the experimental image (Figure 2-II-e). In the diffractogram of the area III (Figure 2-III-d), extra diffraction spots, for example, $11\text{-}1_S$, are apparent, indicating the existence of a spinel structure (denoted with a subscript S). Regardless of the similarity of the HRTEM image of the area III (Figure 2-III-e) and that of the area II, a characteristic pattern with alternating weak and strong contrasts of $(11\text{-}1)_S$ planes is clearly observed. This points to the existence of a spinel structure because only this structure has different atomic densities in the (11-1) cation planes, as shown in Figure 2-III-g. The atomic density for the (11-1) cation plane of the spinel structure marked by the red arrows (A plane) is three times of that marked by the black arrows (B plane) (for the arrangement of the cations in $(012)_R$, $(11\text{-}1)_S$, and $(11\text{-}1)_{RS}$, see Supporting Information, Figure S2). However, the simulation would not match the experimental image if we used only the pure spinel structure. On the basis that the edge of the particle (about 4 nm wide) is dominated by the rock-salt structure (Figure 2-II-e), we assumed that there are two surface layers (about 4 nm thick on the top and bottom of the particle) with the rock-salt structure in area III, while the middle part is the spinel structure. Figure 2-III-f illustrated our calculated image with 4 nm thick rock-salt at the top surface, 2.4 nm thick spinel in the middle, and 3.4 nm thick rock-salt at the bottom surface, resulted in good agreement with the experimental image. On the basis of the above analysis, we conclude that the particle consists of three phases: rhombohedral, spinel, and rock-salt. The rhombohedral phase is the dominated structure and generally in the core of the particle, while the rock-salt structure generally distributes on the surface. The shell (slightly off the surface) is mainly the spinel phase mixed with small amount of rhombohedral phase (see Supporting Information, Figure S3). The overcharged particle can therefore be described by a core−shell-surface structure with rhombohedral in the core, spinel in the shell, and rock-salt structure on the surface. The inset in Figure 2c schematically shows such a core−shell-surface structure. The crystallographic relationship among rhombohedral, spinel, and rock-salt structures are described in the Supporting Information.

After examining many overcharged $Li_xNi_{0.8}Co_{0.15}Al_{0.05}O_2$ particles (several hundreds of particles), we found that most particles have this kind of core−shell-surface structure. The rock-salt surface layer is about a few nanometers, while the spinel shell (mixed with small amount of rhombohedral) ranges from a few nanometers to tens of nanometers. We note that the lattice spacing of the $(11\text{-}1)_{RS}$ should be larger than that of the $(012)_R$ or the $(22\text{-}2)_S$ based on the lattice parameters of the bulk rock-salt structure. However, the HRTEM images (Figure 2c) show that the lattice spacing of the $(11\text{-}1)_{RS}$ is basically the same as that

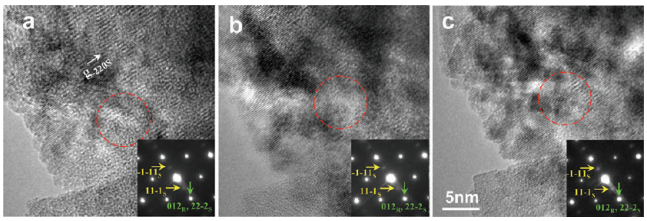

Figure 3. HRTEM images from the particle shown in Figure 2(c) after heating at (a) 100 °C, (b) 200 °C, and (c) 300 °C. The insets are the corresponding SAEDPs from a large area (~240 nm in diameter) of the same particle. The circle in the images marks the same area at different temperatures.

of $(012)_R$, indicating that the lattice parameter of the rock-salt structure on the surface is reduced at room temperature, as a results of the interfacial stress by the spinel and rhombohedral structures. Such a core−shell-surface structure is difficult to detect by XRD.

We also compared the results from XRD and TEM on the overcharged $Li_xNi_{0.8}Co_{0.15}Al_{0.05}O_2$ particles before heating. The XRD data was collected by averaging a sample area in a mm-length scale; only the rhombohedral structure was observed. When we used SAED to probe the sample area in the range of hundreds of nm, the spinel structure was occasionally observed when we selected thin areas (less than 100 nm thick) (see Supporting Information, Figure S4), but most of the time, we saw only the rhombohedral structure. However, HRTEM imaging revealed all three structures, the rhombohedral (located in the core, far from the surface), spinel (the shell near the surface), and rock-salt (at the surface layer or edge of the particle), in the scale range of tens of nm. These three structures can be clearly identified and distinguished by the symmetry of their atomic arrangement (hexagonal dots for rhombohedral, fine lines for rock salt, and alternating contrast lines for spinel) if the sample is correctly orientated in imaging. These three structures were observed simultaneously for the first time on an overcharged sample at room temperature. Their direct identification, with high spatial resolution and location specification provides us powerful tools to follow the nucleation and propagation of the new structure throughout the whole phase-transition process, which is critical for understanding the thermal behaviors of the electrode materials. It demonstrates that, at room temperature, the "high temperature phases", spinel structure (observed in XRD only after heating above 171 °C), and rock-salt structure (observed in XRD only after heating above 262 °C) are nucleated and grown to tens of nm size at the outer shell and surface layer of the overcharged $Li_xNi_{0.8}Co_{0.15}Al_{0.05}O_2$ particles. These "high temperature phases" formed at room temperature by overcharge serve as "seeds" to accelerate the phase transitions to spinel and rock-salt structures during heating, both of which are associated with oxygen loss. Therefore, any methods that would modify the surface structure of the particle with proper control in preventing overcharge, which reduces or eliminates "seed formation" of "high temperature structures", especially the rock-salt structure, will improve the thermal stability of this type of materials.

The local structural evolution of the $Li_xNi_{0.8}Co_{0.15}Al_{0.05}O_2$ particles during heating was monitored in situ. We found that the phase transitions during heating are irreversible, because of the permanent loss of oxygen in high vacuum TEM, and the structures of the sample after cooling back to room temperature remained the same as they had been at high temperatures.

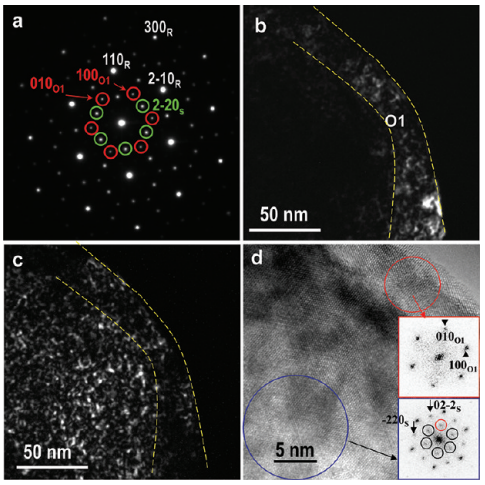

Figure 4. (a) SAEDP of an overcharged $Li_xNi_{1/3}Co_{1/3}Mn_{1/3}O_2$ particle. (b−c) Dark field images using reflections of (b) 100_{O1} and (c) $2\text{-}20_S$. The dashed lines indicate the same position in (b) and (c). (d) HRTEM image from the edge of the particle. The insets at the right-middle and the right-bottom are the diffractograms from the red and blue circled areas, respectively. Note that the reflections marked by the circles in the right-bottom inset are due to the multiscattering effects (e.g., the reflection marked by the red circle can be yielded through -220_S and 100_{O1} double diffraction).

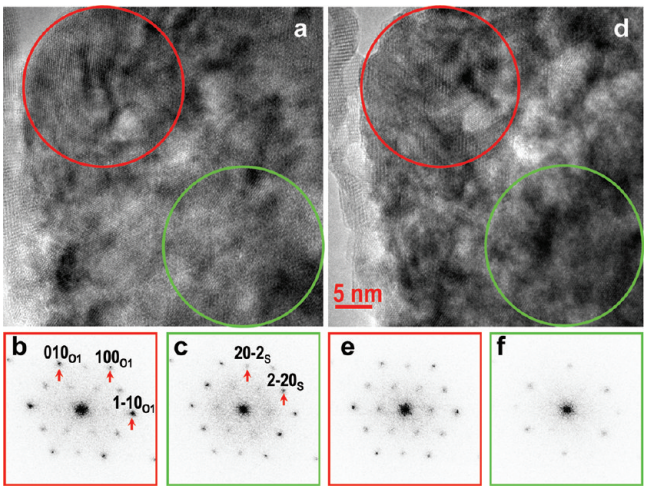

Figure 5. (a) HRTEM image of an overcharged $Li_xNi_{1/3}Co_{1/3}Mn_{1/3}O_2$ particle. (b−c) diffractograms from the (b) red and (c) green circled area in (a). (d) HRTEM image of the same particle after heating at 200 °C. (e−f) diffractograms from the (e) red and (f) green circled area in (d).

Therefore, the images we acquired at room temperature after heating are fully representative of the sample at high temperature. Figure 3 shows the HRTEM images of the sample heated at 100, 200, and 300 °C for 30 min respectively for the same area in Figure 2. After heating at 100 °C (Figure 3a), very weak $11\text{-}1_S$ and $-1\text{-}11_S$ spots in SAEDP appear (inset of Figure 3a), denoting an increase in the spinel phase. The circled area that display a rhombohedral structure at room temperature shows alternative strong- and weak- $(11\text{-}1)_S$ lattice contrast, indicating that they have changed to the spinel structure. After heating at 200 °C (Figure 3b), the intensity of the $11\text{-}1_S$ spot in SAEDP increased slightly. The same area as marked by a circle shows a mixture of weak and strong fringes, similar to that in area III in Figure 2-III. This implies that the circled area consist of spinel- and rock-salt-structures. Heating at 300 °C (Figure 3c), caused the $-1\text{-}11_S$ and $11\text{-}1_S$ spots in SAEDP to strengthen, indicating the overall growth of the spinel phase in the particle. However, at the edge, the spinel phase transformed into the rock-salt phase, as seen in the circled area where the fine $(11\text{-}1)_{RS}$ fringes of the rock-salt phase dominate even though a small number of strong $(11\text{-}1)_S$ fringes of the spinel phase remain. After heating at 400 °C, the circled area was transformed completely to the rock-salt phase, though there were remnants of the spinel phase in some areas. We checked many particles using SAED and HRTEM, confirming that the majority phase is the rock-salt phase after heating at 400 °C.

Overcharged $Li_xNi_{1/3}Co_{1/3}Mn_{1/3}O_2$ Particles. The size of the $Li_xNi_{1/3}Co_{1/3}Mn_{1/3}O_2$ particles is similar to that of the $Li_xNi_{0.8}Co_{0.15}Al_{0.05}O_2$ ones, ranging from hundreds of nanometers to a few micrometers. Unlike the overcharged $Li_xNi_{0.8}Co_{0.15}Al_{0.05}O_2$, there is no trace of the rock-salt structure on the surface. For most particles of the overcharged $Li_xNi_{1/3}Co_{1/3}Mn_{1/3}O_2$, when we tilted the particles to the $[001]_R$ orientation, we observed the reflections that the rhombohedral lattice prohibits. Figure 4a shows the SAEDP of the particle. We indexed the spots with strong intensity by the rhombohedral structure. One set of the weak spots marked by the green circles is indexed as the $[111]_S$ pattern of the spinel structure LiM_2O_4 (M = $Ni_{1/3}Co_{1/3}Mn_{1/3}O_2$). Another set of the weak spots, marked by the red circles, seemingly represent the extinct reflections of the rhombohedral structure, $LiMO_2$, implying a primitive hexagonal structure. We have ruled out the possibility that the weak spots may be caused by the Li ion and vacancy ordering. Our diffraction intensity calculations show that the supperlattice spots due to the Li ion and vacancy ordering would be much weaker than what we observed in Figure 4a because of the weak scattering power of the Li ion. By tilting the sample to the other orientations, we determined that this set of the spots correspond to the CdI_2-type structure MO_2 (denoted as O1) which is formed by the sliding of two-thirds of the MO_2 layers after removal of the Li from the rhombohedral phase.[28] This is consistent with the XRD observation that shows weak O1 peaks. Figure 4b illustrates the dark-field image formed by applying a small aperture to allow only the 100_{O1} reflection to pass through the aperture. Undoubtedly, the O1 phase (bright area) is distributed at the surface of the particle. The dark-field image (Figure 4c) formed by using the $2\text{-}20_S$ reflection demonstrates that the distribution of the spinel phase is slightly off the surface. Figure 4d is the HRTEM image from the edge of the particle. The diffractogram (right-middle inset) from the surface (red circle) has only the reflections of the O1 phase, while that from the area circled by a blue line (right-bottom inset) contains the reflections of both the O1 and the spinel phases. On the basis of these observations, we conclude that most of the overcharged $LiNi_{1/3}Co_{1/3}Mn_{1/3}O_2$ particles have a core−shell-surface structure with the O1 on the surface, the spinel phase in the shell, and the rhombohedral phase in the core. By comparison with the overcharged $Li_xNi_{0.8}Co_{0.15}Al_{0.05}O_2$ at room temperature, the overcharged $Li_xNi_{1/3}Co_{1/3}Mn_{1/3}O_2$ forms a CdI_2-type MO_2 structure at the surface, which protects the particle from losing oxygen.

Figure 5a shows the HRTEM of an overcharged $Li_xNi_{1/3}Co_{1/3}Mn_{1/3}O_2$ particle. The diffractograms from the red- and green-circled areas (Figure 5b and 5c) denote that both areas consist of

dx.doi.org/10.1021/cm201452q |*Chem. Mater.* 2011, 23, 3953–3960

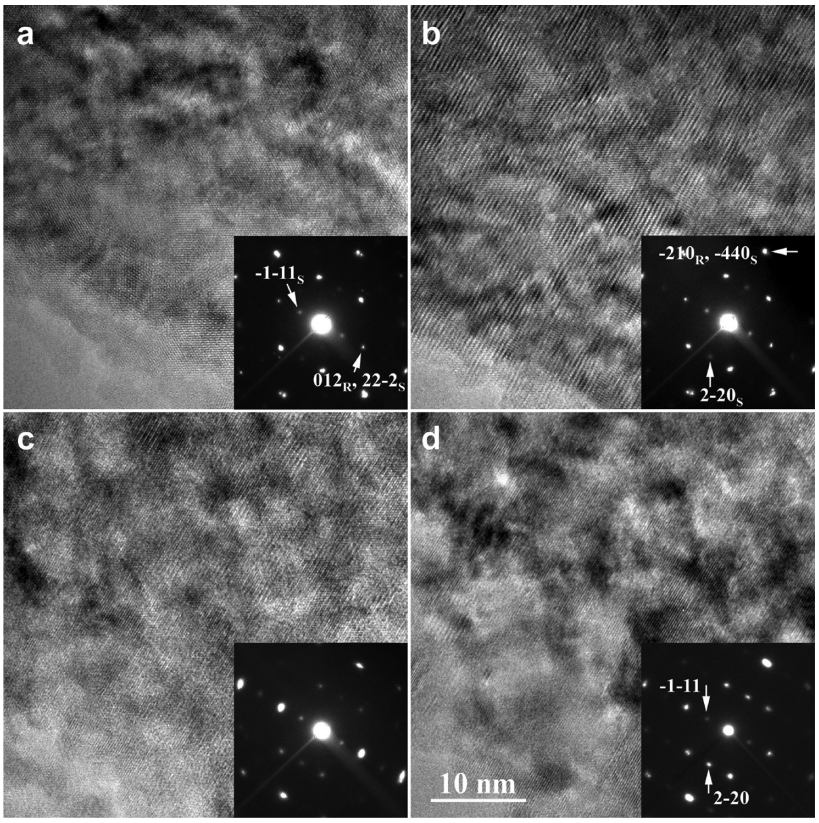

Figure 6. HRTEM images taken from an overcharged $Li_xNi_{1/3}Co_{1/3}Mn_{1/3}O_2$ particle. (a) Before heating. (b−d) After heating at (b) 100 °C, (c) 400 °C, and (d) 500 °C. The insets are the corresponding SAEDPs taken from large area (~240 nm in diameter) of the same particle. Each SAEDP consists of $[-1-21]_R$ and $[112]_S$ patterns (subscripts R and S represent the rhombohedral and spinel phase, respectively). The overlapped spots, for example, 012_R and $22\text{-}2_S$, -210_R and -440_S, are labeled by two index.

the O1 and spinel phases. After heating at 200 °C, the structure changes (Figure 5d). The green-circled area has transformed to the M_3O_4-type spinel structure, as evidenced by the disappearance of the diffraction spots of the O1 in the diffractogram (Figure 5f). In the red-circled area, the O1 remains, the intensities of most of the O1 spots in the diffractogram weaken (Figure 5e), while those of the spinel become stronger than they were before heating (Figure 5b), indicating that part of the O1 phase changed into the M_3O_4 type spinel phase. The O1 phase disappeared after heating the sample above 300 °C. The formation of the O1 phase, rather than the rock-salt structure, at the surface of the particle is crucial in protecting the particle from losing oxygen. Moreover, the formation of the M_3O_4 type spinel phase from the O1 phase may seed the transition from the LiM_2O_4 type spinel to the M_3O_4 type spinel at high temperatures. In contrast, for the $Li_xNi_{0.8}Co_{0.15}Al_{0.05}O_2$, the removal of the Li during overcharge entails the loss of oxygen at the surface, because of the formation of the rock-salt structure. The rock-salt structures at the surface of the $Li_xNi_{0.8}Co_{0.15}Al_{0.05}O_2$ particles formed by overcharge serve as seeds for phase transition during heating, so easing the transformation from the spinel structure to the rock-salt structure, and resulting in poor thermal stability.

Figure 6a shows the HRTEM image of a particle with the beam direction along $[-1-21]_R$ direction at room temperature. The rhombohedral- and spinel-phases are present. The SAEDP (inset of Figure 6a) acquired from the particle's larger area (~240 nm in diameter) also shows weak reflections of the spinel structure, for example, $11\text{-}1_S$ and $-1\text{-}11_S$ spots. After heating at 100 °C, the edge of the particle changes to the spinel structure (Figure 6b). The spinel phase grows, extending to the core of the particle as the temperature increased. Starting at about 400 °C, the rock-salt phase appeared at the surface of the particle, as shown in Figure 6c. More of the rock-salt phase forms after heating at 500 °C, but the spinel phase persists, even at the edge. The SAEDP from the larger area (inset of Figure 6d) clearly reveals the reflections of the spinel structure. Interestingly, at 500 °C, the intensity of $-1\text{-}11_S$ weakens, while that of $2\text{-}20_S$ strengthens in comparison with those exposed to temperatures below 500 °C. This agrees very well with the time-resolved X-ray observations, indicating the formation of M_3O_4 type spinel structure M_3O_4, in which the tetrahedral sites (8a) are occupied by Ni, Co, and Mn ions; in contrast, they were occupied by Li^+ only in the regular LiM_2O_4 -type spinel. Apparently, the formation of the M_3O_4 type spinel-structure pushes the formation of the rock-salt structure to higher temperatures, and resulted in the improvement of the thermal stability of the material. We attribute the formation of the M_3O_4 type spinel and its stability over a wider temperature range compared with the $Li_xNi_{0.8}Co_{0.15}Al_{0.05}O_2$ sample to the Co and Mn concentration. It is well-known that Ni^{4+} is highly unstable and is easily reduced to Ni^{2+} to form NiO. On the other hand, Mn^{4+} is quite stable, as evidenced by the naturally existing MnO_2. In the $Li_xNi_{1/3}Co_{1/3}Mn_{1/3}O_2$ sample, Mn is mostly in the Mn^{4+} state. Therefore, even after all the Li^+ are removed during overcharge, and all of the Ni and Co ions are reduced to Ni^{2+} and Co^{2+}, the system still remains stabilized in

the $(Ni^{2+}_{1/3}Co^{2+}_{1/3}Mn^{4+}_{1/3})_3O_4$ type of structure with the average oxidation state of $M^{8/3+}$, similar to the M_3O_4 type spinel.

(c). First Principles Calculations. During charging and overcharging cycles, the Li ions diffuse from the core to the surface of the particles. The distribution of the Li ion in the particle is likely not uniform with concentration gradient between the core and the surface. It has been reported that the decomposition reaction of Li_xMO_2 (M = Ni, Co, or Mn) at different Li ion concentration differs significantly.[29] For layered Li_xNiO_2, it decomposes into spinel $LiNi_2O_4$ and layered $LiNiO_2$ at high Li concentration (e.g., $0.5 < x < 1$), while it decomposes into spinel $LiNi_2O_4$ and rock-salt NiO with release of O_2 at low Li concentration (e.g., $x < 0.5$).[29] For Li_xCoO_2, it decomposes to spinel $LiCo_2O_4$ and layered $LiCoO_2$ at high Li concentration, but decomposes to spinel $LiCo_2O_4$, and spinel Co_3O_4 and O_2 at low Li concentration. For Li_xMnO_2, spinel $Li_{0.5}MnO_2$ and layered MnO_2 were found to be energetically stable.[30] As we mentioned above, during charge the core of the nanoparticles are expected to have higher Li concentration, thus the layered structure Li_xMO_2 (M = $Ni_{0.8}Co_{0.15}Al_{0.05}$ for $Li_xNi_{0.8}Co_{0.15}Al_{0.05}O_2$, M = $Ni_{1/3}Co_{1/3}Mn_{1/3}$ for $Li_xNi_{1/3}Co_{1/3}Mn_{1/3}O_2$) is preferred. As Li concentration decreases from core to the shell, the spinel structure appears to be energetically stable. At the surface, the Li concentration is close to zero, the rock-salt structure and layered O1 structure are therefore expected for Ni-rich $Li_xNi_{0.8}Co_{0.15}Al_{0.05}O_2$ and Co−Mn-rich $Li_xNi_{1/3}Co_{1/3}Mn_{1/3}O_2$ particles, respectively.

The different surface structure for $Li_xNi_{0.8}Co_{0.15}Al_{0.05}O_2$ and $Li_xNi_{1/3}Co_{1/3}Mn_{1/3}O_2$ particles was further clarified by our first principle calculations for the following oxidation reaction:

$$2MO_2\ (\text{layered, O1}) \rightarrow 2MO\ (\text{rocksalt}) + O_2 \qquad (1)$$

where M represents a transition metal such as Ni, Co, and Mn, or their related alloys. The reaction enthalpy for the above reaction can be written as

$$\Delta H = 2E(MO) + E(O_2) - 2E(MO_2) \qquad (2)$$

where, the $E(MO)$, $E(O_2)$, and $E(MO_2)$ are forming energies of MO, O_2, and MO_2, respectively. Here, the negative reaction enthalpy means that it is exothermic for MO_2 to decompose to rock-salt MO with release of O_2, implying that the rock-salt structure is more stable. In contrast, the positive enthalpy indicates that the MO_2 is more stable than MO. By considering the inclusions of the correction for binding energy of O_2 molecule, 1.36 eV/O_2, and the correction of GGA+U treatments (with U = 6.4 eV for Ni, 3.3 eV for Co, and 3.5 eV for Mn),[31] we obtained the averaged reaction enthalpy $\Delta H \sim -0.8$ eV per O_2 for M = $Ni_{0.8}Co_{0.2}O_2$ and $\Delta H \sim +1$ eV per O_2 for M = $Ni_{1/3}Co_{1/3}Mn_{1/3}O_2$, respectively. The negative enthalpy for M = $Ni_{0.8}Co_{0.2}O_2$ points out that it is thermodynamically stable to form a rock-salt MO structure for Ni-rich compound, while the positive enthalpy for M = $Ni_{1/3}Co_{1/3}Mn_{1/3}O_2$ indicates that the layered MO_2 with O1 structure is energetically favorable. The origin for the enhanced stability of O1-structure MO_2 at the surface for $Li_xNi_{1/3}Co_{1/3}Mn_{1/3}O_2$ particles is mainly from the large energy required for decomposing MnO_2 ($\sim +3$ eV/O_2) into MnO, comparing with CoO_2 ($\sim +1.7$ eV/O_2) and NiO_2 (~ -1.5 eV/O_2) cases. In contrast, the formation of rock-salt MO at the surface for the overcharged $Li_xNi_{0.8}Co_{0.15}Al_{0.05}O_2$ particles is largely due to the negative reaction enthalpy of $2NiO_2 \rightarrow 2NiO + O_2$. Therefore, from the energetic point of view, to enhance the thermal stability of the layered Li_xMO_2 against decomposition of MO_2 when overcharged, it is suggested to decrease the Ni concentration, while increasing the Mn concentration of the Li_xMO_2 particles. To obtain the high energy density, it would be desirable to make the material Mn rich at the surface and Ni rich in the bulk.

CONCLUSIONS

We studied the structural changes of overcharged $Li_xNi_{0.8}Co_{0.15}Al_{0.05}O_2$ and $Li_xNi_{1/3}Co_{1/3}Mn_{1/3}O_2$ cathode materials during heating using combined time-resolved XRD, in situ TEM, and first principles calculations. We observed a complex structure with a rhombohedral core, the spinel shell, and the rock-salt structure at the surface for the overcharged $Li_xNi_{0.8}Co_{0.15}Al_{0.05}O_2$ particles at room temperature. Heating the sample in the microscope, the spinel phase propagates toward the core of the particle. Meanwhile, the rock-salt phase grows toward the spinel phase region. After heating at 400 °C, most particles transform into the rock-salt phase. For overcharged $Li_xNi_{1/3}Co_{1/3}Mn_{1/3}O_2$, at room temperature, the surface is the CdI_2-type structure, rather than the rock-salt-type structure which changes to the M_3O_4 type spinel phase in elevated temperatures. Heating the sample transforms the rhombohedral structure in the core to the spinel structure, which then transforms into the M_3O_4 type spinel, and pushes the formation of the rock-salt phase to much higher temperatures than that for $Li_xNi_{0.8}Co_{0.15}Al_{0.05}O_2$. On the other hand, the delithiation of $Li_xNi_{0.8}Co_{0.15}Al_{0.05}O_2$ during overcharge causes the loss of oxygen at the surface because of the formation of the rock-salt structure. The rock-salt structure at the surface of the $Li_xNi_{0.8}Co_{0.15}Al_{0.05}O_2$ particle formed by overcharge serves as nucleation center for the phase transition, thereby easing the transformation from the spinel structure to the rock-salt structure, and resulting in poor thermal stability. Our study suggests that Mn plays a major rule in suppressing the formation of the rock-salt structure on the surface. Therefore, increasing the Mn content on the surface of the particles might be an effective way to improve the thermal stability of the layered cathodes, while retaining the high energy density by keeping high Ni concentration in the bulk.

ASSOCIATED CONTENT

Supporting Information. Calculated XRD for LiM_2O_4 type and M_3O_4 type spinel structures, crystallographic relationship among rhombohedral, spinel, and rock-salt structures, and additional TEM images. This material is available free of charge via the Internet at http://pubs.acs.org.

AUTHOR INFORMATION

Corresponding Author
*E-mail: xyang@bnl.gov (X.-Q.Y.), zhu@bnl.gov (Y.Z.).

ACKNOWLEDGMENT

The work was supported by the U.S. Department of Energy, Office of Basic Energy Science, and the Assistant Secretary for Energy Efficiency and Renewable Energy, Office of Vehicle Technologies, under the program of Vehicle Technology Program, under Contract no. DEAC02-98CH10886. Xiaojian Wang is supported by the Northeastern Center for Chemical Energy

Storage, an Energy Frontier Research Center funded by the U.S. Department of Energy, Office of Science, Office of Basic Energy Sciences under Contract no. DE-SC0001294 (Contract no. for BNL: DEAC02-98CH10886). J.-C.Z. is supported by SRFDP no. 20090121120028, and the Natural Science Foundation of Fujian Province, China (Grant 2009J01015).

REFERENCES

(1) Tarascon, J. M.; Armand, M. *Nature* **2001**, *414* (6861), 359–367.
(2) Guilmard, M.; Croguennec, L.; Denux, D.; Delmas, C. *Chem. Mater.* **2003**, *15* (23), 4476–4483.
(3) Yabuuchi, N.; Kim, Y. T.; Li, H. H.; Shao-Horn, Y. *Chem. Mater.* **2008**, *20* (15), 4936–4951.
(4) Yoon, W. S.; Balasubramanian, M.; Yang, X. Q.; McBreen, J.; Hanson, J. *Electrochem. Solid-State Lett.* **2005**, *8* (2), A83–A86.
(5) Yoon, W. S.; Hanson, J.; McBreen, J.; Yang, X. Q. *Electrochem. Commun.* **2006**, *8* (5), 859–862.
(6) Yoon, W. S.; Balasubramanian, M.; Chung, K. Y.; Yang, X. Q.; McBreen, J.; Grey, C. P.; Fischer, D. A. *J. Am. Chem. Soc.* **2005**, *127* (49), 17479–17487.
(7) Yoon, W. S.; Chung, K. Y.; McBreen, J.; Zaghib, K.; Yang, X. Q. *Electrochem. Solid-State Lett.* **2006**, *9* (9), A415–A417.
(8) Zeng, D. L.; Cabana, J.; Yoon, W. S.; Grey, C. P. *Chem. Mater.* **2010**, *22* (3), 1209–1219.
(9) Key, B.; Bhattacharyya, R.; Morcrette, M.; Seznec, V.; Tarascon, J. M.; Grey, C. P. *J. Am. Chem. Soc.* **2009**, *131* (26), 9239–9249.
(10) Debart, A.; Dupont, L.; Poizot, P.; Leriche, J. B.; Tarascon, J. M. *J. Electrochem. Soc.* **2001**, *148* (11), A1266–A1274.
(11) Weaving, J. S.; Coowar, F.; Teagle, D. A.; Cullen, J.; Dass, V.; Bindin, P.; Green, R.; Macklin, W. J. *J. Power Sources* **2001**, *97−8*, 733–735.
(12) Lee, K. K.; Yoon, W. S.; Kim, K. B.; Lee, K. Y.; Hong, S. T. *J. Power Sources* **2001**, *97−8*, 308–312.
(13) Arai, H.; Okada, S.; Sakurai, Y.; Yamaki, J. *Solid State Ionics* **1998**, *109* (3−4), 295–302.
(14) Belharouak, I.; Lu, W. Q.; Vissers, D.; Amine, K. *Electrochem. Commun.* **2006**, *8* (2), 329–335.
(15) Belharouak, I.; Vissers, D.; Amine, K. *J. Electrochem. Soc.* **2006**, *153* (11), A2030–A2035.
(16) Wang, Y. D.; Jiang, J. W.; Dahn, J. R. *Electrochem. Commun.* **2007**, *9* (10), 2534–2540.
(17) Myung, S. T.; Lee, K. S.; Yoon, C. S.; Sun, Y. K.; Amine, K.; Yashiro, H. *J. Phys. Chem. C* **2010**, *114* (10), 4710–4718.
(18) Muto, S.; Sasano, Y.; Tatsumi, K.; Sasaki, T.; Horibuchi, K.; Takeuchi, Y.; Ukyo, Y. *J. Electrochem. Soc.* **2009**, *156* (5), A371–A377.
(19) Abraham, D. P.; Twesten, R. D.; Balasubramanian, M.; Kropf, J.; Fischer, D.; McBreen, J.; Petrov, I.; Amine, K. *J. Electrochem. Soc.* **2003**, *150* (11), A1450–A1456.
(20) Abraham, D. P.; Twesten, R. D.; Balasubramanian, M.; Petrov, I.; McBreen, J.; Amine, K. *Electrochem. Commun.* **2002**, *4* (8), 620–625.
(21) Abraham, D. P.; Liu, J.; Chen, C. H.; Hyung, Y. E.; Stoll, M.; Elsen, N.; MacLaren, S.; Twesten, R.; Haasch, R.; Sammann, E.; Petrov, I.; Amine, K.; Henriksen, G. *J. Power Sources* **2003**, *119*, 511–516.
(22) Ohzuku, T.; Makimura, Y. *Chem. Lett.* **2001**, *7*, 642–643.
(23) Shaju, K. M.; Bruce, P. G. *Adv. Mater.* **2006**, *18* (17), 2330–+.
(24) Belharouak, I.; Lu, W. Q.; Liu, J.; Vissers, D.; Amine, K. *J. Power Sources* **2007**, *174* (2), 905–909.
(25) Sun, Y. K.; Myung, S. T.; Park, B. C.; Prakash, J.; Belharouak, I.; Amine, K. *Nat. Mater.* **2009**, *8* (4), 320–324.
(26) Giannozzi, P.; Baroni, S.; Bonini, N.; Calandra, M.; Car, R.; Cavazzoni, C.; Ceresoli, D.; Chiarotti, G. L.; Cococcioni, M.; Dabo, I.; Dal Corso, A.; de Gironcoli, S.; Fabris, S.; Fratesi, G.; Gebauer, R.; Gerstmann, U.; Gougoussis, C.; Kokalj, A.; Lazzeri, M.; Martin-Samos, L.; Marzari, N.; Mauri, F.; Mazzarello, R.; Paolini, S.; Pasquarello, A.; Paulatto, L.; Sbraccia, C.; Scandolo, S.; Sclauzero, G.; Seitsonen, A. P.; Smogunov, A.; Umari, P.; Wentzcovitch, R. M. *J. Phys.: Condens. Matter* **2009**, *21* (39), 395502.
(27) Nam, K. W.; Yoon, W. S.; Yang, X. Q. *J. Power Sources* **2009**, *189* (1), 515–518.
(28) Arai, H.; Tsuda, M.; Saito, K.; Hayashi, M.; Takei, K.; Sakurai, Y. *J. Solid State Chem.* **2002**, *163* (1), 340–349.
(29) Wang, L.; Maxisch, T.; Ceder, G. *Chem. Mater.* **2007**, *19* (3), 543–552.
(30) Mishra, S. K.; Ceder, G. *Phys. Rev. B* **1999**, *59* (9), 6120–6130.
(31) Wang, L.; Maxisch, T.; Ceder, G. *Phys. Rev. B* **2006**, *73* (19), 195107.